

Modeling and Analysis the Effect of PZT Area on Square Shaped Substrate for Power Enhancement in MEMS Piezoelectric Energy Harvester*

Babak Montazer[†] and Utpal Sarma[‡]

*Department of Instrumentation and USIC, Gauhati University,
Guwahati, Assam 781014, India*

[†]babakmontazer@gauhati.ac.in

[‡]utpalsarma@gauhati.ac.in

Received 5 May 2016

Accepted 27 December 2016

Published 27 February 2017

Modeling and analysis of a MEMS piezoelectric (PZT-Lead Zirconate Titanate) unimorph cantilever with different substrates are presented in this paper. Stainless steel and Silicon (110) are considered as substrate. The design is intended for energy harvesting from ambient vibrations. The cantilever model is based on Euler–Bernoulli beam theory. The generated voltage and power, the current density, resonance frequencies and tip displacement for different geometry (single layer and array structure) have been analyzed using finite element method. Variation of output power and resonant frequency for array structure with array elements connected in parallel have been studied. Strain distribution is studied for external vibrations with different frequencies. The geometry of the piezoelectric layer as well as the substrate has been optimized for maximum power output. The variation of generated power output with frequency and load has also been presented. Finally, several models are introduced and compared with traditional array MEMS energy harvester.

Keywords: PZT; MEMS; energy harvester; vibration; cantilever.

1. Introduction

Development of efficient methods for extracting unused energy from ambient sources to replace chemical cell in micro-power autonomous system is a growing research activity. The rapid growth of micro-systems and its implementation in wireless and autonomous sensors accelerate research in such fields. The mechanical vibrations are found abundantly in our surrounding.¹ Conversion of this vibrational energy into usable electrical power is achieved by three means: electrostatic, electromagnetic and piezoelectric.² Piezoelectric method is considered to be more efficient than other two

*This paper was recommended by Regional Editor Piero Malcovati.

[†] Corresponding author.

mechanisms because of its high electromechanical coupling effect, self-generating nature and capability of generating power in the range of μW to mW .³ The advent of MEMS fabrication process and recently introduced NEMS provide an efficient way to achieve fabrication of piezoelectricity based micro energy harvester. Studies on various designs of MEMS piezoelectric energy harvester have been reported in Ref. 4.

A simple model of piezoelectric energy harvester has been reported in Ref. 5. The model is based on the mass-spring system and the outcome shows the dissipation of power affected due to damping of the system. Shen *et al.*⁶ successfully fabricated a unimorph PZT cantilever generator that can generate $2.15 \mu\text{W}$ from vibration with a magnitude of $2g$ ($g = 9.81 \text{ ms}^{-2}$) at a resonance frequency about 461.5 Hz . Fang *et al.*⁷ used nickel metal mass to tune the resonance frequency at about 608 Hz , which generates $0.89 \text{ V}_{\text{peak-peak}}$. Lin *et al.*⁸ constructed a PZT (MEMS) harvesting device of micrometer size based on silicon and stainless steel substrate. The device, based on stainless steel has maximum output power of $34 \mu\text{W}$ with $1.5g$, however, PZT layer based on silicon provides $21 \mu\text{W}$ power at $1.5g$. Most of the energy obtainable from such devices lie around the resonant frequency.⁹ Liu *et al.*¹⁰ investigated array of piezoelectric cantilevers with different proof mass. Liu *et al.*,¹¹ fabricated and simulated array of PZT patterned on the cantilever and connected in parallel and series with low operating frequency and the result shows more power generated in the parallel connection.

The design and development of different models based on MEMS energy harvester with PZT as a piezoelectric material is presented in this work. The models are compared in single PZT prototype and array of PZT based on stainless steel and silicon (110) material as substrate. The models are simulated and analyzed using Finite Element Method (FEM). The models are also simulated repeatedly to optimize the best geometry and dimension for obtaining maximum power. The dependency on other parameters like strain, variation of resonance frequency as well as behavior of current density in piezoelectric material has also been reported.

2. Problem Formulation

The constitutive relation of a piezoelectric material can be expressed by the following equations

$$D_3 = d_{31}T_1 + \varepsilon_0\varepsilon_{33}^T E_3, \quad (1)$$

$$\xi_1 = s_{11}^E T_1 + d_{31} E_3, \quad (2)$$

where ξ_1 and T_1 are the strain and stress vectors along the length of a piezoelectric material. D_3 and E_3 denote the z -coordinates of the electric displacement and electric field, respectively. The d_{31} and $\varepsilon_0\varepsilon_{33}^T$ are the piezoelectric constants and electrical permittivity whereas s_{11}^E specifies the component of compliance under constant electric field.

By considering (1) and (2), mechanical stress is found to be a function of electric displacement. Therefore, electric displacement affects the movement of charge on the piezoelectric plate. The electric field will be created across the top and bottom electrodes in the thickness direction due to the mechanical strain on the piezoelectric material. In case of piezoelectric cantilever vibration the electrodes can be coupled with load resistances from zero to infinity, i.e., from short circuit to open circuit.

The short circuit and open circuit conditions can be calculated by assuming $E_3 = 0$ or $D_3 = 0$ in (1) or (2). When $D_3 = 0$ we have infinite value of load resistance connected across piezoelectric electrodes.¹² For the estimation of the short-circuit it is assumed $E_3 = 0$.

Here, (3) is the Euler–Bernoulli relation for the proposed model.¹³ The direction of external force is along the z -direction where c_{air} is the air damping coefficient, c_{strain} is the strain of material damping coefficient and YI is equivalent bending stiffness.

$$\begin{aligned}
 YI \frac{\partial^4 u(x, t)}{\partial x^4} + I c_{\text{strain}} \frac{\partial^5 u(x, t)}{\partial x^4 \partial t} + c_{\text{air}} \frac{\partial u(x, t)}{\partial t} + m \frac{\partial^2 u(x, t)}{\partial t^2} \\
 = -[m + m_t \delta(x - l)] \frac{\partial^2 u_b(x, t)}{\partial t^2} .
 \end{aligned} \tag{3}$$

δ is the Dirac delta function. The forcing term due to external damping is neglected in this model.

$$u_b(x, t) = g(t) + xh(t), \tag{4}$$

$u_b(x, t)$ is the base displacement given by (4) where $g(t)$ is the translation in the z -direction and $h(t)$ is the rotational displacement which is neglected in this model, so $h(t) = 0$.

The forcing function may be expressed as

$$f(t) = -m \left[\frac{\partial^2 g(t)}{\partial t^2} \int_0^l U_n(x) dx \right] - m_t U_n(l) \frac{\partial^2 g(t)}{\partial t^2}, \tag{5}$$

where $u(x, t)$ is the lateral position of the beam from the center which can be determined as

$$u(x, t) = \sum_{n=1}^{\infty} U_n(x) T_n(t). \tag{6}$$

The vertical displacement of the clamped-free beam with respect to time for the n th mode is obtained as

$$T_n(t) = \frac{m\omega^2 - j\omega c_{\text{air}}}{\omega_n^2 - \omega^2 + j2\xi_n \omega_n \omega} \frac{\sigma}{k_n l} \sqrt{\frac{l}{m}}, \tag{7}$$

where the total damping ratio is $\xi_n = \xi_{\text{Strain}} + \xi_{\text{air}}$, $\xi_{\text{Strain}} = C_{\text{strain}} I \omega_n / 2YI$ and $\xi_{\text{air}} = C_{\text{air}} / 2m\omega_n$.

When damping is neglected in (3) the modified Euler–Bernoulli relation can be expressed as

$$\frac{\partial^4 U_n(x)}{\partial x^4} - k_n^4 U(x) = 0. \tag{8}$$

The following boundary conditions are considered for the system as $x = 0, u(0, t) =$

$$0, \left[\frac{\partial u(x,t)}{\partial x} \right]_{x=0} = 0 \text{ and at } x = l: \left[YI \frac{\partial u^2(x,t)}{\partial x^2} \right]_{x=l} = \left[YI \frac{\partial u^3(x,t)}{\partial x^3} \right]_{x=l} = 0$$

$$U_n(x) = C_r [\cos(k_n x) - \cosh(k_n x) + \sigma(\sin(k_n x) - \sinh(k_n x))], \tag{9}$$

$$\sigma = \frac{\sin(k_n l) - \sinh(k_n l) + (k_n l) \frac{m_t}{m} (\cos(k_n l) - \cosh(k_n l))}{\cos(k_n l) + \cosh(k_n l) - (k_n l) \frac{m_t}{m} (\sin(k_n l) - \sinh(k_n l))}, \tag{10}$$

where k_n is the wavenumber in spatial coordinate, $k_n^4 = m\omega_n^2/YI$, $k_n l = \nu_n$, $m = \rho_p t_p + \rho_s t_s$ and $m_t = \rho_m t_m$, m and m_t is the mass per unit length where ρ_p, ρ_s, t_p and t_s are the densities of the piezoelectric material, substrate, the thickness of piezoelectric layer and substrate, respectively. m_t/m is a dimensionless parameter which gives the proof mass to beam mass ratio.

By considering (7), (8) and (9), one can obtain the relative tip displacement for a harmonically excited beam with a proof mass attached to its free end as

$$u(x, t) = 2\omega^2 A_0 \cos(\omega t) \sum_{n=1}^{\infty} [\cos(k_n x) - \cosh(k_n x) + \sigma(\sin(k_n x) - \sinh(k_n x))] \times \frac{m\omega^2 - j\omega c_{air}}{\omega_n^2 - \omega^2 + j2\xi_n \omega_n \omega} \frac{\sigma}{k_n l} \sqrt{\frac{l}{m}}. \tag{11}$$

2.1. Cantilever resonance frequency

The resonant frequency of MEMS cantilever depends on the structure of the cantilever and the type of the material which can be represented as¹²

$$f_n = \frac{\nu_n^2}{2\pi l^2} \sqrt{\frac{YI}{\left(\frac{4l_m}{l} + 3\right) m_t}}. \tag{12}$$

Here ν_n is the n th mode eigenvalue with $n = 1, 2, 3, \dots$ and $\nu_1 = 1.87, \nu_2 = 4.69, \nu_3 = 7.85$ and so on.

For negligible thickness of the electrode layers, the stiffness depends on the thickness of the substrate and piezoelectric layer. Moreover, tip displacement and beam deformation are reduced in bulky multilayer.

The appropriate neutral axis point for composite two beams can be expressed by

$$\bar{z} = \frac{w_s t_s z_s + \eta_e w_p t_p z_p}{w_s t_s + \eta_e w_p t_p}. \tag{13}$$

It is obvious from Eq. (13) that if the substrate thickness is zero, the neutral axis lies in the middle of the piezoelectric layer. This creates equal and opposite strains on the top and bottom surface of the piezoelectric layer. This condition results in perfect charge cancellation inside the piezoelectric layer and power generated will be zero.

When the thickness of the substrate increases, the distance of the neutral axis moves gradually out of the piezoelectric layer. This causes unequal strains on the surfaces of the piezoelectric layers, hence, a net charge appears across the layers. If the substrate is relatively thicker, then the total deflection of the beam will be reduced which will cause less charge generation. So, for maximum charge generation, the thickness of the substrate needs to be optimized. Here \bar{z} is the neutral axis position of the beam (Fig. 1) and z_s, z_p are the heights of the centroid in substrate and piezoelectric layer, respectively, i.e., $z_s = (t_s/2) + t_p$ and $z_p = t_p/2$.

The Elastic modulus of the PZT (E_{lp}) and Elastic modulus of the substrate (E_{ls}) are written as

$$E_{lp} = E_p(1 - \nu_p), \tag{14}$$

$$E_{ls} = E_s(1 - \nu_s), \tag{15}$$

where E_p, E_s, ν_p and ν_s are piezoelectric Young's modulus, substrate Young's modulus, piezo Poisson's ratio and substrate Poisson's ratio, respectively.

The ratio of Elastic modulus is $\eta_e = E_{lp}/E_{ls}$. The equivalent moment of inertia of the composite beam (I) about the neutral axis can be represented as

$$I = \frac{w_p t_p^3}{12} + w_p t_p (z_p - \bar{z})^2 + \frac{w_s t_s^3}{12} + w_s t_s (z_s - \bar{z})^2, \tag{16}$$

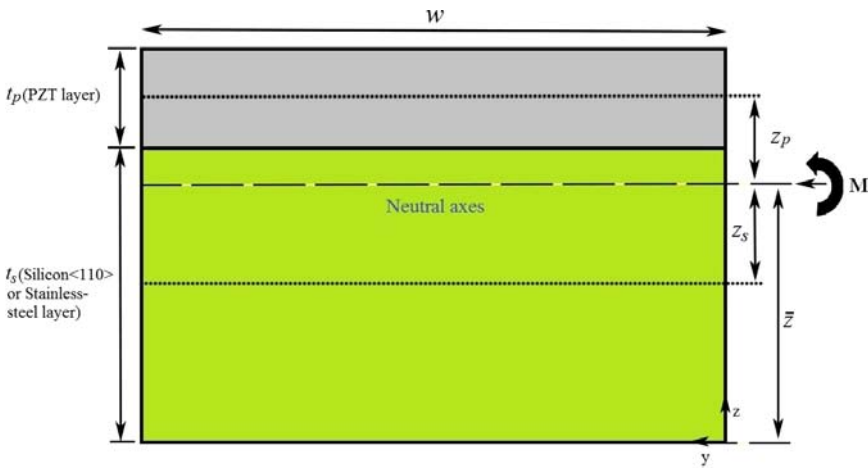


Fig. 1. Schematic of neutral axis position in cantilever beam.

where w_p and w_s are the width of PZT and substrate layer, respectively. Thus, the flexural rigidity of the composite beam is expressed as

$$YI = E_p w_p t_p \left[(z_p - \bar{z})^2 + \frac{t_p^3}{12} \right] + E_s w_s t_s \left[(z_s - \bar{z})^2 + \frac{t_s^3}{12} \right], \quad (17)$$

The strain distribution in a multilayered piezoelectric sheet in terms of elastic modulus of the composite beam is written as

$$S_x = -z_p \frac{\partial^2 u(x, t)}{\partial x^2}. \quad (18)$$

2.2. Voltage and power generation

The z component electrical displacement D_3 , can be represented as¹⁴

$$D_3 = d_{31} E_p \frac{\partial^2 u(x, t)}{\partial x^2} (\bar{z} - z_p). \quad (19)$$

By applying Gauss's law on rectangular geometry, total stress-induced charge Q_p , created on the top and bottom of the piezoelectric surface during vibration and can be expressed as¹⁵

$$Q_p = \int_0^{l_p} \int_0^{w_p} D_3 dx dy = d_{31} E_p \int_0^{l_p} \int_0^{w_p} \left[\frac{\partial^2 u(x, t)}{\partial x^2} (\bar{z} - z_p) \right] dx dy, \quad (20)$$

$$q_p = \frac{Q_p}{T} = \alpha d_{31} E_p \int_0^{l_p} \int_0^{w_p} \left[\frac{\partial^2 u(x, t)}{\partial x^2} (\bar{z} - z_p) \right] dx dy. \quad (21)$$

Here q_p is the stress-charge with respect to surface where α is a correction factor that resulted from FEM simulation. It is a summation of all stress charges generated in piezoelectric layer. T is the amplitude of beam vibration.

The capacitance C_p of the active layer can be expressed as

$$C_p = \varepsilon_0 \varepsilon_{33}^T \frac{w_p l_p}{t_p}. \quad (22)$$

Open circuit voltage across the electrodes of piezoelectric layer can be expressed by

$$V_{oc} = \frac{Q_p}{C_p} = d_{31} E_p \frac{t_p}{w_p l_p \varepsilon_0 \varepsilon_{33}^T} \int_0^{l_p} \int_0^{w_p} \left[\frac{\partial^2 u(x, t)}{\partial x^2} (\bar{z} - z_p) \right] dx dy. \quad (23)$$

For maximum power transfer, piezoelectric impedance $|Z_p|$ is

$$|Z_p| = \frac{1}{2\pi f_n C_p} = R_{Load}. \quad (24)$$

The current I_L at the load due to harmonic oscillation is given by

$$I_L = \frac{V_{oc}}{Z_p + Z_L}, \quad (25)$$

where Z_p and Z_L are considered as complex impedance of the piezoelectric capacitor and connected load, respectively.

For an array of n piezoelectric elements the load voltage V_L and load power P across a load of z_L is expressed as

$$V_L = \frac{Z_L}{\frac{1}{n} Z_p + Z_L} n V_{oc}, \quad (26)$$

$$P = \frac{V_L^2}{Z_L} = \frac{(n V_{oc})^2 Z_L}{\left(\frac{1}{n} Z_p + Z_L\right)^2}. \quad (27)$$

3. Design and Construction

The unimorph structure of the cantilever with a single piezoelectric patch and array of piezoelectric patch are shown in Figs. 2(a) and 2(b). All models consist of a bulk

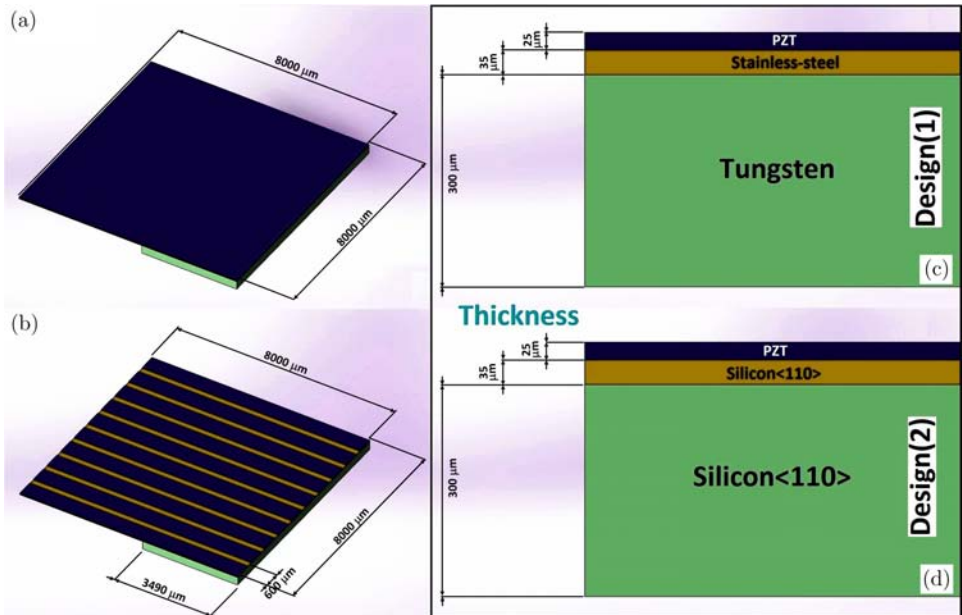


Fig. 2. (a) Single Piezo patch (SPP) (b) Array Piezo patch (APP) for different design (c) cross-section of design(1) (d) cross-section of design(2).

Table 1. Dimension parameters used for the simulation and analysis.

Substrate ($l \times w \times t$)	Cases ($l \times w \times t$) number of array	Resonance Frequency (Hz) based on S-s or Si		Proof mass ($l \times w \times t$)
		S-s	Si	
Stainless-steel(S-s) or Silicon(110)(Si) ($8000 \mu\text{m} \times 8000 \mu\text{m} \times 35 \mu\text{m}$)	Case1			Stainless-steel(S-s) or Silicon(110)(Si) ($3490 \mu\text{m} \times 8000 \mu\text{m} \times 300 \mu\text{m}$)
	• Array Piezoelectric patch(APP), ($8000 \mu\text{m} \times 600 \mu\text{m} \times 25 \mu\text{m}$)10	164	396	
	• Single piezoelectric patch (SPP), ($8000 \mu\text{m} \times 8000 \mu\text{m} \times 25 \mu\text{m}$)	178	422	
	Case2			
	• Array piezoelectric Patch (APP), ($1600 \mu\text{m} \times 600 \mu\text{m} \times 25 \mu\text{m}$)10	132	332	
	• Single piezoelectric patch (SPP), ($1600 \mu\text{m} \times 8000 \mu\text{m} \times 25 \mu\text{m}$)	137	345	

Lead Zirconate Titanate (PZT) in d_{31} mode. The thickness of the electrode layers are very thin, so their geometrical effects are ignored in the model. In the first design, stainless-steel is considered as substrate, tungsten as proof mass and PZT is used as piezoelectric material as shown in Fig. 2(c). In the second design, Silicon $\langle 110 \rangle$ is used for both substrate and proof mass and PZT is used as piezoelectric material as shown in Fig. 2(d). All the structures are optimized at their resonance frequencies. Details of the structure and first frequency modes are given in Table 1. Mechanical and electrical properties of the beam are given in Table 2. One end of the cantilever is fixed and constrained to the vibrator $A_0 \cos(\omega t)$ with low acceleration ($1g$).

Table 2. Material property used for optimization and analysis.

Mechanical and electrical properties	PZT5H	Si(110)	Stainless-steel	W (Tungsten)
Density (Kg/m^3)	7,500	2,330	7,850	19,350
E (GPa)	62	169	200	400
Poisson's ratio	0.27	0.064	0.29	0.28
Piezo.coefficients d_{31} (C/N)	-274	—	—	—
Piezo.coefficients d_{33} (C/N)	650	—	—	—
Piezo.coefficients d_{15} (C/N)	741	—	—	—
Constant stress dielectric ϵ_{11}	3,130	—	—	—
Constant stress dielectric ϵ_{22}	3,130	—	—	—
Constant stress dielectric ϵ_{33}	3,800	—	—	—

4. Results

Figures 3(a)–3(d) show the output voltages (peak to peak) of APP(Case1), APP (Case2), SPP(Case1) and SPP(Case2), respectively for both designs. Cantilevers are simulated as per the mentioned geometry at resonance frequency and the load impedance is considered to be $300\text{ k}\Omega$. APP(Case2) has a peak-voltage of 2.33 V which is higher than the other structures. In addition, the voltage generated in APPS-s(Case2) is more than that of the APPSi(Case2) which is true for other three geometries also.

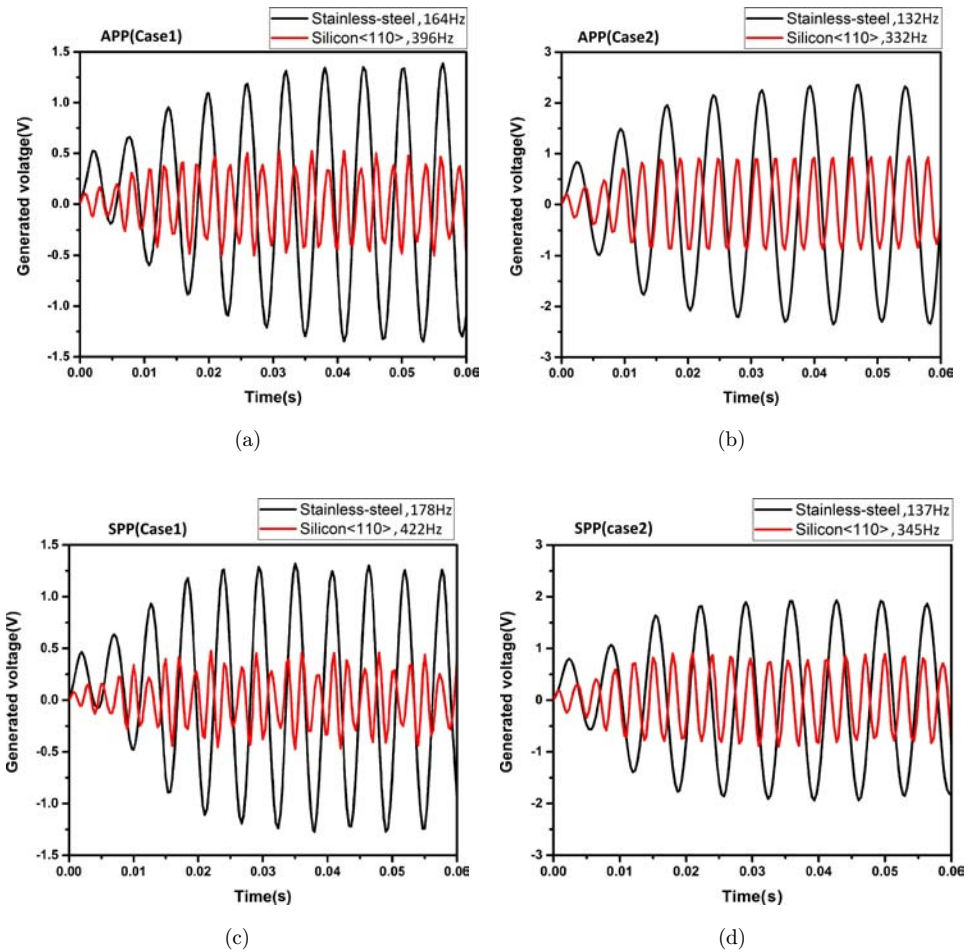


Fig. 3. (a) (b) (c) and (d) are transient analysis of APP(Case1), APP(Case2), SPP(Case1) and SPP (Case2), respectively.

4.1. Load impedance analysis

Figure 4 shows the variation of power with load for all structures as shown in Fig. 2. The output power has a maximum value of $32.1 \mu\text{W}$ for SPPS-s (Case1) and $25.7 \mu\text{W}$ for APPS-s(Case1). The detailed findings are presented in Table 3. The load resistance for maximum power is different for different geometries which establishes Eqs. (22)–(25). The power generation in APPSi (Case2) (10 PZT connected in parallel), decreases because of deflection in Silicon $\langle 110 \rangle$ as well as electromechanical coupling of PZT and Silicon. Figure 5 shows width optimization for array element over a fixed substrate area where power increases to $34.8 \mu\text{W}$ at $750 \mu\text{m}$ width which is more than SPPS-s(Case1).

4.2. Investigation of output power for array of piezoelectric patch connected in parallel

The variation of output power with excitation frequency at a fixed load of $300 \text{ k}\Omega$ for APPS-s(Case2) is shown in Fig. 6 with piezoelectric elements connected in parallel. A

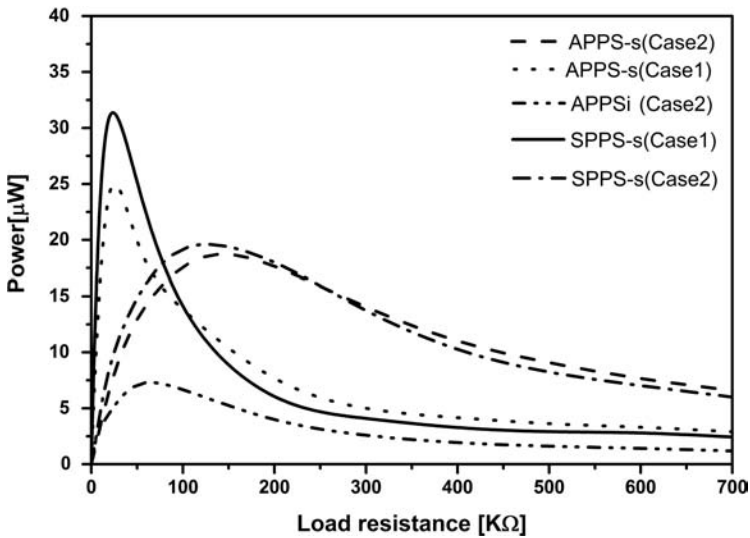


Fig. 4. Power delivered to the load for different samples.

Table 3. The maximum power extracted at optimum load resistances for different PZT geometry.

Geometry	Load impedance (kΩ)	Resonant frequency (Hz)	Voltage (V_p)	Power (μW)
APPS-s(Case1)	20	164	0.716	25.7
APPS-s(Case2)	120	132	1.46	17.8
SPPS-s(Case1)	17	178	0.73	32.1
SPPS-s(Case2)	110	137	1.43	18.8
APPSi(Case2)	51	332	0.63	7.9

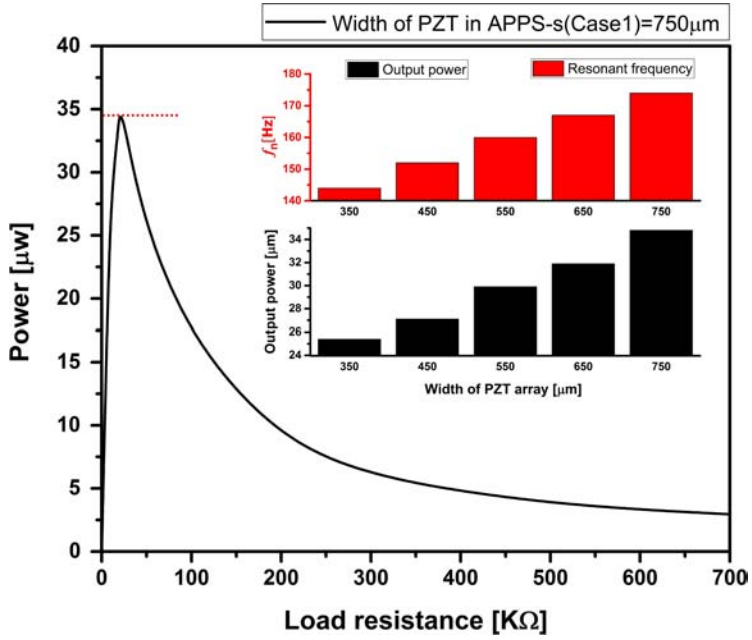


Fig. 5. Optimal width for array piezoelectric energy harvester.

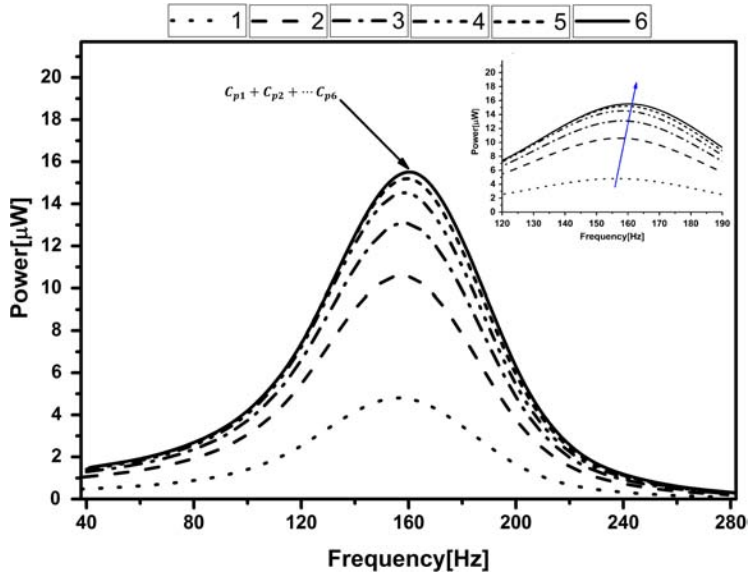


Fig. 6. Power against frequencies for number of PZT elements connected in parallel.

shift of the resonant frequency toward higher side is observed as the number of piezoelectric elements connected in parallel increase. It is also observed that power increases gradually with the number of elements connected in parallel and remains constant after an optimum value, as shown in Fig. 6. This variation is in conformity with Eq. (27). This shift of the resonance frequency is due to the effect of electrical stiffness and electrical damping of PZT, which can be explained on the basis of the equivalent lumped model of PZT as shown in Fig. 7 with the dynamic equations as

$$M\ddot{u} + C_m\dot{u} + K_m u - \theta v = -A_0\omega^2 \cos(\omega t), \tag{28}$$

$$Q = \theta u + C_p v, \tag{29}$$

where $M = m_{\text{proof}} + (1/3)m_p$ is the approximate effective of mass, C_m is the mechanical damping part, K_m and Q are the mechanical stiffness electric charge, respectively. The coupling coefficient (θ) of rectangular PZT patch can be expressed as

$$\theta = E_p d_{31} z_p \int_0^l \int_0^w \left[\frac{\partial^2 u(x, t)}{\partial x^2} \right] dx dy. \tag{30}$$

The electrical damping is given as

$$\xi_e = \frac{K^2}{2} \left(\frac{\phi}{\left(\frac{\omega}{\omega_n}\right)^2 \phi^2 + 1} \right). \tag{31}$$

Here K is the electromechanical coupling coefficient and $K^2 = \theta/K_m(nC_p)$. $\phi = \omega_n Z_L nC_p$ is a dimensionless factor for time constant, ω_n is the natural frequency of the system. The electrical stiffness (K_{el}) is represented by

$$K_{el} = \frac{K^2}{2} \left(\frac{\left(\frac{\omega}{\omega_n}\right)^2 \phi^2}{\left(\frac{\omega}{\omega_n}\right)^2 \phi^2 + 1} \right). \tag{32}$$

The value of ϕ increases with the number of PZT elements connected in parallel.

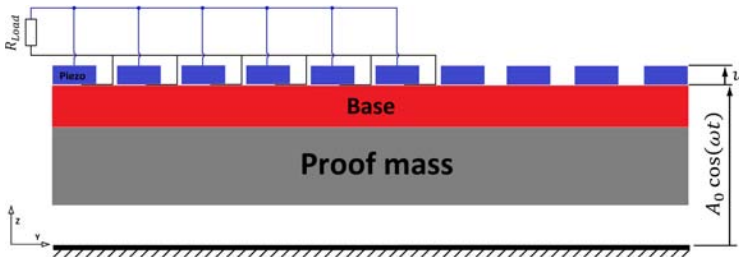


Fig. 7. 1D lumped model of APP.

4.3. The analysis of strain

Figures 8(a) and 8(b) show the variation of strain with axial beam length obtained by simulation for SPPS-s and SPPSi, respectively for Case1, whereas (c), (d) are those for SPPS-s and SPPSi, respectively, for Case2. A section of a two-layered cantilever/piezoelectric laminate is considered and simulated in frequency domain. From Fig. 8, it is observed that when resonance frequency matches with natural frequency, then strain distribution as well as tip displacement reaches maximum value along the length. Strain created over the upper plane of the cantilever is dependent on tip displacement. By comparing all the strain distribution observations, it can be realized that SPPSi for Case2 is stiffer than the other samples, this is because of the material property of silicon.

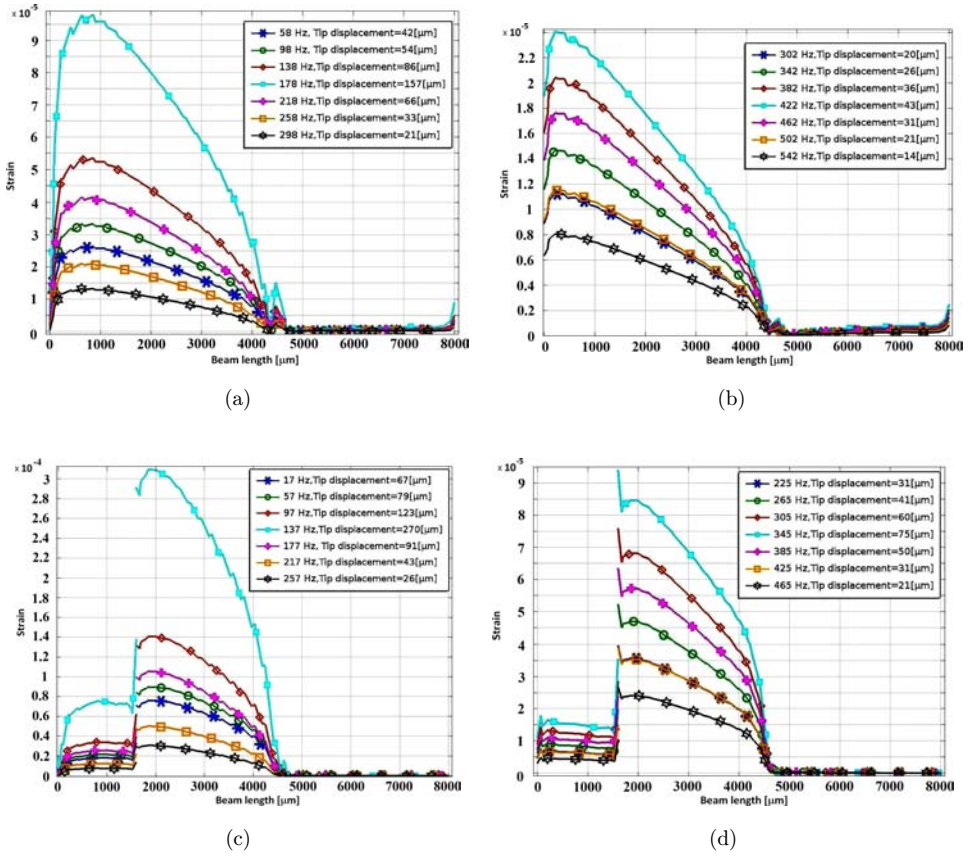


Fig. 8. Strain distribution generated over the surface of cantilevers (a) SPPS-s Case1 (b) SPPSi Case1 (c) SPPS-s Case2 and (d) SPPSi Case2.

4.4. Transient and frequency analysis

The deflection of the beam along the length (x -axis) for all points continuously over the surface of the substrate is shown in Fig. 9. The curve is obtained by a transient time analysis where the beam reaches the maximum deflection toward upward direction. For sample (1), APPS-s ($l_p = 8000 \mu\text{m}$) deflection is maximum as compared with other samples. However, for APPSi ($l_p = 1600 \mu\text{m}$), the magnitude of displacement is minimum. This is because of the effect of mechanical properties of substrates and density of proof mass.

Figure 10 shows the distribution of current densities for different structures with stainless-steel material as a substrate. It is observed that the maximum current density is generated near the fixed end of the beam. The stress charge distribution as presented in (21) is directly related to the current density. In the location of proof mass, stiffness is higher which provides minimum current density. Current density in SPP and APP (Case2) is around 40% lesser than SPP and APP (Case1) at high stress charge concentration area. The output power, resonant frequency and tip displacement variation are investigated by optimizing the area of PZT keeping the substrate area constant ($8,000l \times 8,000w$) μm^2 and with the condition $l = w$. The maximum output power is achieved at 0.25 PZT/substrate ratio Fig. 11(a). The maximum power is obtained when PZT impedance matches with the load impedance. Additionally, resonance frequency and tip displacement trend increases and

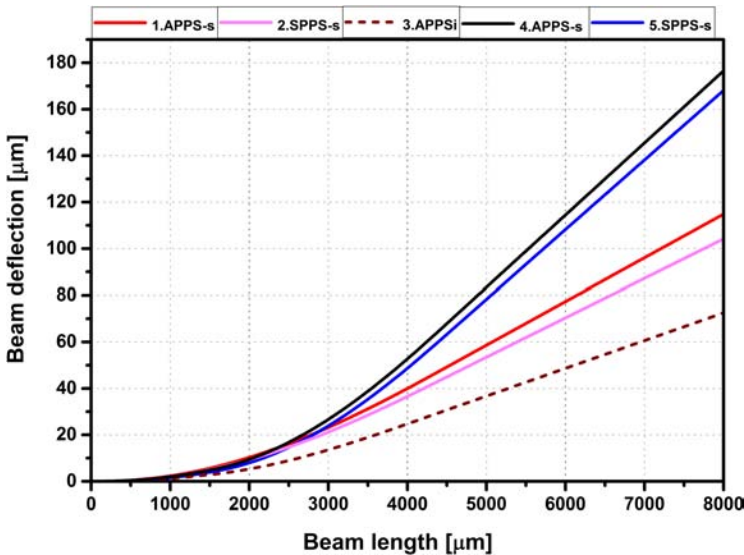


Fig. 9. (1,2,3,4-5) is the analysis of bending displacement (1.APPS-s, 2.SPPS-s and 3.APPSi, respectively for Case1 whereas 4.APPS-s, 5.SPPS-s, respectively, for Case2).

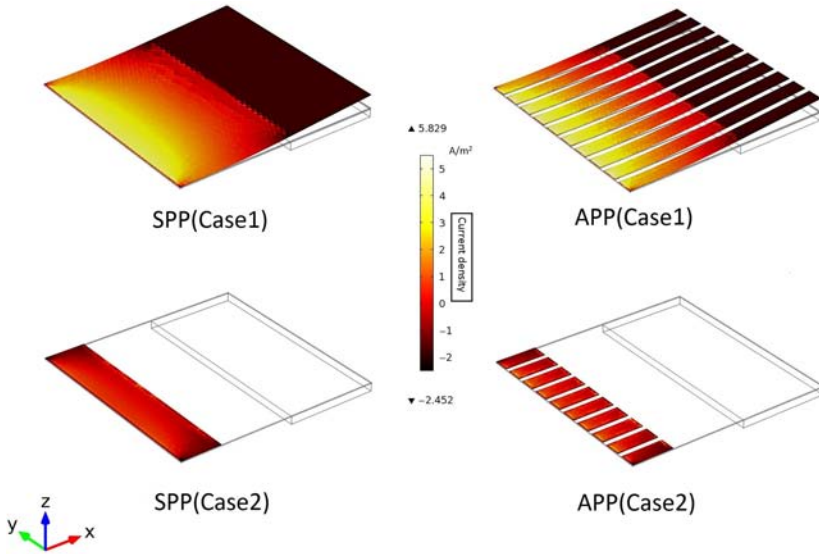


Fig. 10. Simulation result of current density of different PZT geometry.

decreases, respectively for increasing PZT area. Figure 12 shows result of maximum power in SPPS-s and APPS-s at the same ratio of area (0.25) is $48.5 \mu\text{W}$ at 148 Hz and $43.85 \mu\text{W}$ at 153 Hz, respectively.

The variation of resonant frequency, tip displacement and output power with beam length for constant proof mass length and PZT length of $1600 \mu\text{m}$ is shown in Fig. 11(b). Maximum power is achieved when the substrate length is three times that of l_p . The frequency is maximum when $(l - l_m - l_p)$ is minimum which makes the ratio $l_p/(l - l_m)$ equal to unity keeping the thicknesses and proof mass constant. Resonance frequency increases with the decrease in l (Eq. (12)) as the stiffness of the composite cantilever increases.¹² In addition, the power output of the harvester

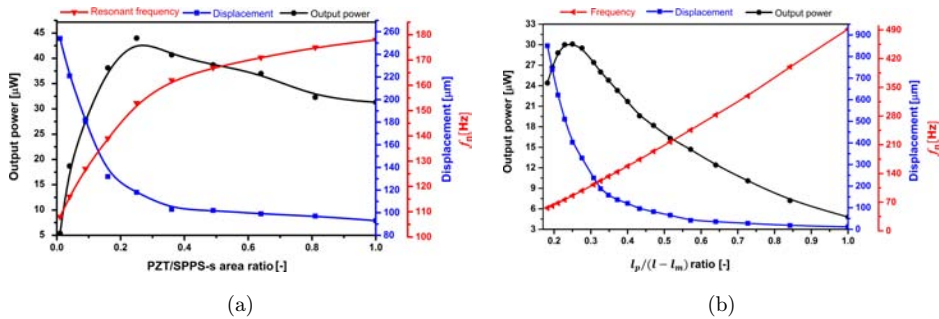


Fig. 11. FEM simulation for power, resonance frequency and displacement at 1g, versus (a) PZT/SPPS-s area ratio (b) PZT/Stainless-steel length ratio.

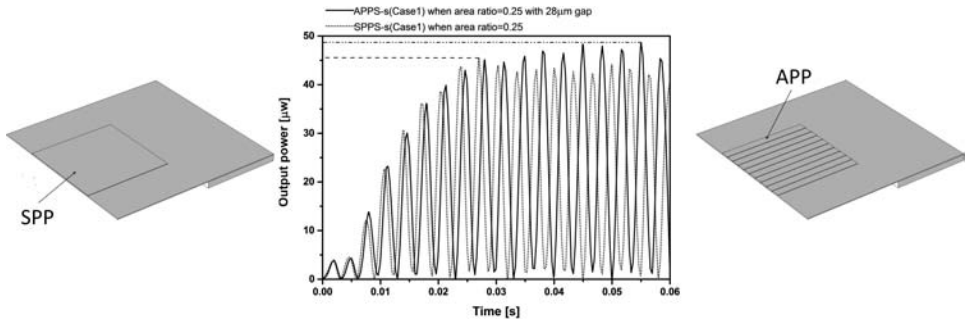


Fig. 12. Transient analysis of power when PZT/substrate area ratio is 0.25 for SPPS-s and APPS-s.

depends on centroid strain. By increasing the length, the position of centroid can be changed over the substrate.

Figure 13(a) illustrates the output voltage and resonant frequency as a function of PZT length over fixed substrate length. From the figure, it can be seen that the voltage and frequency response do not change uniformly with the length of PZT layer. It is found that the open circuit voltage increases with the length and reaches a maximum and then decreases. The maximum open circuit voltage is obtained at PZT length of 1.6 mm and the resonant frequency is maximum at 4.0 mm as shown in Fig. 13(a) for SPPSi. However, in Fig. 13(b) SPPS-s the maximum values are obtained at 3.2 mm and at 4.4 mm for open circuit voltage and resonant frequency, respectively.

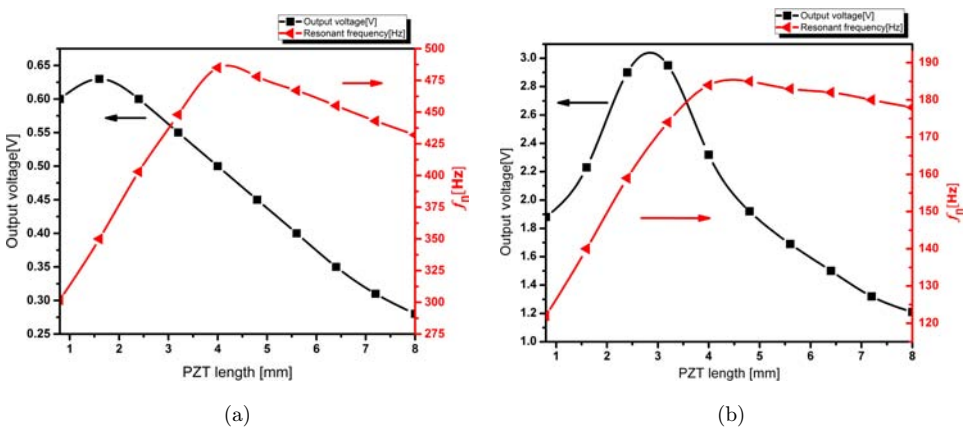


Fig. 13. Simulation results for variation of frequency and voltage for open circuit analysis when increasing the length of the PZT over cantilever (a) SPPSi and (b) SPPS-s.

4.4.1. Array patch optimization (To enhance the power of the design the array patch optimization has been carried out)

Table 4 involves the design optimization of six APPS-s geometric (model 1–6) where the original width of the array geometry is set to 750 μm on stainless steel substrate and tungsten as proof mass integrated with the cantilever. Table 5 includes models (APPSi) with same PZT element arrangements designed according to Ref. 9. The model 1 in Table 5 is designed with approximately equal dimension to the original dimensions. The PZT array pattern is fabricated on silicon substrate and uses the same material as proof mass. The width of the array is 240 μm and length rearrangement is given in Table 4. The power density comparison is shown in Fig. 14(a) for all models it is shown in Tables 4 and 5.

From Table 5, it is observed that the output power increases from 0.0133 μW to 0.0157 μW (model 1 and 3), which means an increase of about 18.04% as compared to the original design in Ref. 9 at 0.1 g acceleration. The volume of the device gets reduced from 10.22 mm³ to 10.21 mm³. The resonant frequency shifted from 35.13 Hz

Table 4. Optimum APPS-s models by considering $w_p = 750 \mu\text{m}$.

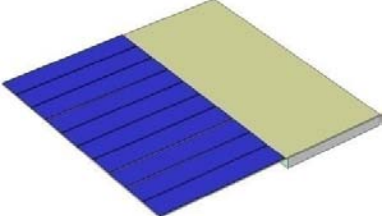
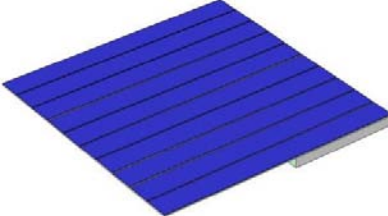
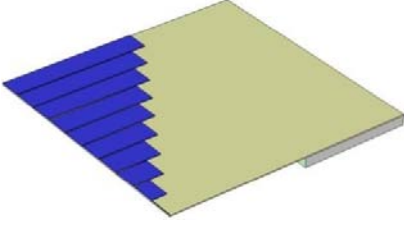
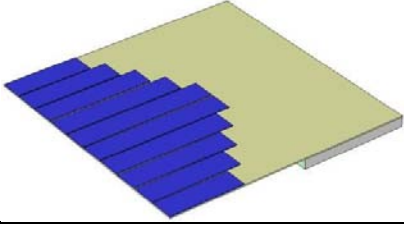
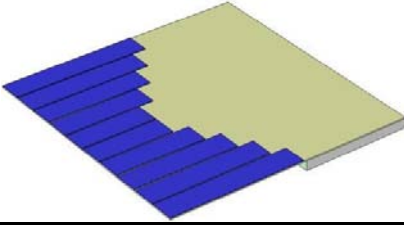
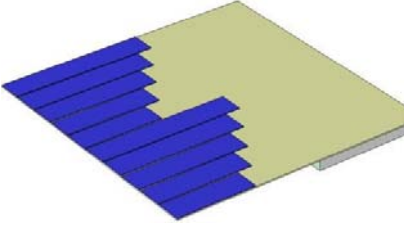
Case index (APPS-s)	Design of array and optimal design variables	Effective Volume	f_n	Power	Power density
		mm^3	Hz	μW	$\mu\text{W g}^{-2} \text{mm}^{-3}$
Model1		11.14	180.6	38.2	3.43
Length (μm)	$l_{p1} = l_{p2} = \dots l_{p10}$ 4400				
Model2		12.12	174.4	36.5	3.01
Length (μm)	$l_{p1} = l_{p2} = \dots l_{p10}$ 8000				

Table 4. (Continued)

Model3		11.03	150.9	41.45					3.75	
Length (μm)	l_{p1}	l_{p2}	l_{p3}	l_{p4}	l_{p5}	l_{p6}	l_{p7}	l_{p8}	l_{p9}	l_{p10}
	4401	3912	3423	2934	2445	1956	1467	978	489	9
Model4		11.26	171.8	39.5					3.50	
Length (μm)	l_{p1}	l_{p2}	l_{p3}	l_{p4}	l_{p5}	l_{p6}	l_{p7}	l_{p8}	l_{p9}	l_{p10}
	2445	2934	3423	3912	4401	4401	3912	3423	2934	2445
Model5		11.26	171.3	38.5					3.41	
Length (μm)	l_{p1}	l_{p2}	l_{p3}	l_{p4}	l_{p5}	l_{p6}	l_{p7}	l_{p8}	l_{p9}	l_{p10}
	4401	3912	3423	2934	2445	2445	2934	3423	3912	4401
Model6		11.26	171.4	38.8					3.44	
Length (μm)	l_{p1}	l_{p2}	l_{p3}	l_{p4}	l_{p5}	l_{p6}	l_{p7}	l_{p8}	l_{p9}	l_{p10}
	4401	3912	3423	2934	2445	4401	3912	3423	2934	2445

to 31.33 Hz in accordance with the change in volume of the device as stated earlier. Model 3 shows the highest power density as compared to five different models in both APPS-s and APPSi. However, APPS-s cantilevers have better performance than those based on silicon in Ref. 9.

Table 5. Optimum APPSi models by considering $w_p = 240 \mu\text{m}$.

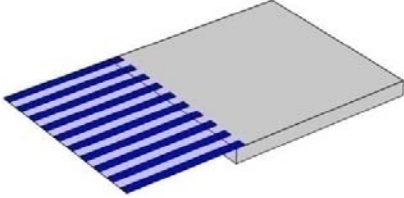

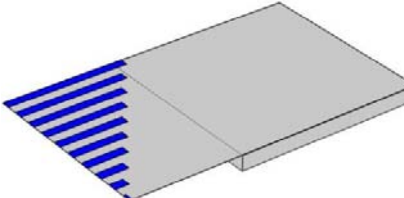
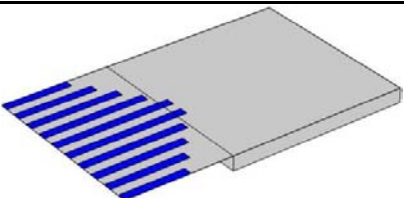
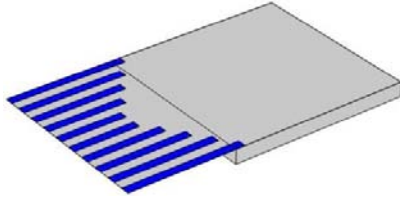
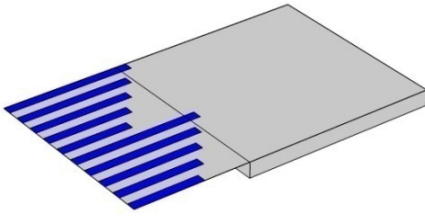
Case index (APPSi)	Design of array and optimal design variables	Effective Volume	f_n	Power	Power density
		mm^3	Hz	μW	$\mu\text{W g}^{-2} \text{mm}^{-3}$
Model1 Ref. 9		10.23	35.13	0.0133	0.13
Length (μm)	$l_{p1} = l_{p2} = \dots l_{p10}$ 3260				
Model2		10.26	36.81	0.0088	0.085
Length (μm)	$l_{p1} = l_{p2} = \dots l_{p10}$ 8000				
Model3		10.21	31.33	0.0157	0.154
Length (μm)	l_{p1} l_{p2} l_{p3} l_{p4} l_{p5} l_{p6} l_{p7} l_{p8} l_{p9} l_{p10} 3259 2897 2535 2173 1811 1448 1086 724 362 72				
Model4		10.22	33.97	0.0156	0.152
Length (μm)	l_{p1} l_{p2} l_{p3} l_{p4} l_{p5} l_{p6} l_{p7} l_{p8} l_{p9} l_{p10} 1811 2173 2535 2897 3259 3259 2897 2535 2173 1811				

Table 5. (Continued)

Model5										
										
		10.22	33.16	0.0156	0.152					
Length	l_{p1}	l_{p2}	l_{p3}	l_{p4}	l_{p5}	l_{p6}	l_{p7}	l_{p8}	l_{p9}	l_{p10}
(μm)	3259	2897	2535	2173	1811	1811	2173	2535	2897	3259
Model6										
										
		10.22	33.96	0.0157	0.153					
Length	l_{p1}	l_{p2}	l_{p3}	l_{p4}	l_{p5}	l_{p6}	l_{p7}	l_{p8}	l_{p9}	l_{p10}
(μm)	3259	2897	2535	2173	1811	3259	2897	2535	2173	1811

The optimal model (Model-3) shows an 8.5% improvement in terms of power output as compared to model 1 (APPS-s). In the designs (as shown in Tables 4 and 5) the generated power is different due to different strains on PZT and substrate layers. Figure 14(b) shows the average surface strain distribution, where the strain obtained between PZT and substrate along the width and length of all arrays assuming 100 bin split between PZT and substrate interface in FEM. From Fig. 14(b) it is clear

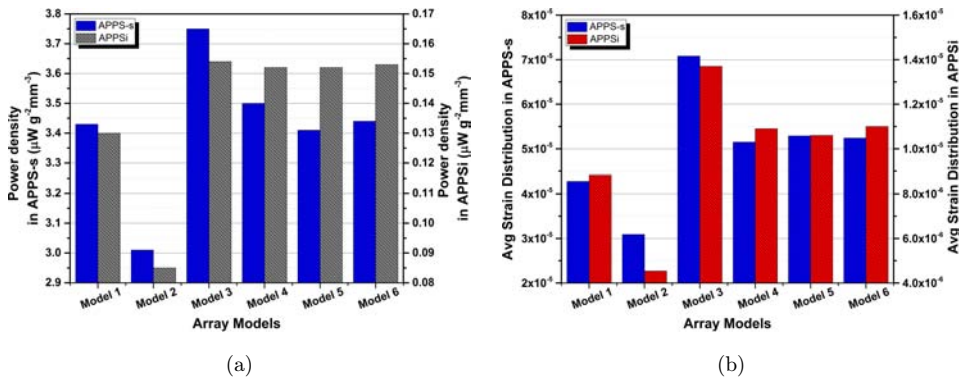


Fig. 14. The various array model of APPS-s, APPSi versus (a) Power density (b) Average strain distribution.

J CIRCUIT SYST COMP Downloaded from www.worldscientific.com by Mr. Siamak Mir Shahri on 02/28/17. For personal use only.

that model 3 gives the highest value of average strain distribution as compared to other models available in Tables 4 and 5. This justifies that the maximum average strain distribution provides maximum charge on piezoelectric. The average strain in model 2 for APPS-s is 129% less than that in model 3; which is 201% for APPSi. The average strain distribution is related to the power output in each model.

5. Conclusion

In this paper, designing, modeling, analysis and optimization of different structures of piezoelectric energy harvester with different substrate material has been explained. The FEM is used to validate the model based on Euler–Bernoulli beam theory.

When the number of elements of PZT patch, connected in parallel fashion increases, power increases steadily and the rate decreases with higher numbers of elements. It is found both in simulation and in the analytical model that the resonant frequency shifts toward higher side with number of elements. Power increases with decreasing space between the array elements or increasing the width of the array elements, which is advantageous than a single piezoelectric patch. The arrays profiled on stainless-steel and silicon cantilever are optimized for getting maximum power density. This will reduce the cost of the prototype harvester. This type of optimization has not been reported so far.

This work establishes the dependence of power output on the ratio of the PZT area over the constant substrate area for both SPPS-s and APPS-s cantilevers (Fig. 11).

From the strain distribution analysis (Fig. 8), it is concluded that the strain on the beam is dependent on both material of the substrate and geometry of PZT.¹⁶ The variation of tip displacement for different excitation frequencies have been reported. In future work, it the bandwidth of MEMS energy harvester will be tried to optimize which is an important factor to capture energy in a wide range of ambient vibrations.

Acknowledgments

We acknowledge Dr. Roy P. Paily, Professor, Dept. of EEE, IITG (Indian Institute of Technology Guwahati) for his valuable suggestions, encouragement and technical supports in this work. Dr. P.K. Boruah, Professor (Retd.), Department of Instrumentation and USIC, Gauhati University has also been acknowledged for his kind support and encouragement.

References

1. M. S. M. Soliman, E. M. Abdel-Rahman, E. F. El-Saadany and R. R. Mansour, A wideband vibration-based energy harvester, *J. Micromech Microeng.* **18** (2008) 115021, doi: 10.1088/0960-1317/18/11/115021.

2. R. Elfrink, T. M. Kamel, M. Goedbloed, S. Matova, D. Hohlfeld, Y. V. Anel and R. V. Schaijk, Vibration energy harvesting with aluminum nitride-based piezoelectric devices, *J. Micromech. Microeng.* **19** (2009) 094005, doi: 10.1088/0960-1317/19/9/094005.
3. Y. Hua, Z. Jielin, D. Licheng and W. Zhiyu, A vibration-based MEMS piezoelectric energy harvester and power conditioning circuit, *Sensors* **14** (2014) 3323–3341, doi: 10.3390/s140203323.
4. S. Priya and D. Inman, *Energy Harvesting Technologies* (Springer, New York, 2009), pp. 39–89.
5. C. B. Williams and R. B. Yates, Analysis of a micro-electric generator for microsystems, *Sens. Actuators A* **52** (1996) 5–11, doi: 10.1016/0924-4247(96)80118-X.
6. D. Shen, J. H. Park, J. Ajitsaria, S. Y. Choe, H. C. Wickle and D. J. Kim, The design, fabrication, and evaluation of a MEMS PZT cantilever with an integrated Si proof mass for vibration energy harvesting, *J. Micromech. Microeng.* **18** (2008) 055017, doi: 10.1088/0960-1317/18/5/055017.
7. H. B. Fang, J. Q. Liu, Z. Y. Xu, L. Dong, L. Wang, D. Chen, B. C. Cai and Y. Liu, Fabrication and performance of MEMS-based piezoelectric power generator for vibration energy harvesting, *Microelectron. J.* **37** (2006) 1280–1284.
8. S. C. Lin and W. J. Wu, Fabrication of PZT MEMS energy harvester based on silicon and stainless steel substrates utilizing an aerosol deposition method, *J. Micromech. Microeng.* **23** (2013) 125028, doi: 10.1088/0960-1317/23/12/125028.
9. H. Liu, C. J. Tay, C. Quan, T. Kobayashi and C. Lee, Piezoelectric MEMS energy harvester for low-frequency vibrations with wideband operation range and steadily increased output power, *J. Microelectromech. Syst.* **20** (2011) 1131–1142, doi: 10.1109/JMEMS.2011.2162488.
10. J. Q. Liu, H. B. Fang, Z. Y. Xu, X. H. Mao, X. C. Shen, D. Chen, H. Liao and B. C. Cai, A MEMS-based piezoelectric power generator array for vibration energy harvesting, *Microelectron. J.* **39** (2008) 802–806.
11. H. Liu, C. Quan, C. J. Tay, T. Kobayashi and L. Chengkuo, A MEMS-based piezoelectric cantilever patterned with PZT thin film array for harvesting energy from low frequency vibrations, *Int. Conf. Physics Procedia, ICOPEN* **19** (2011) 129–133, doi: 10.1016/j.phpro.2011.06.136.
12. T. M. Kamal, R. Elfrink, M. Renaud, D. Hohlfeld, M. Goedbloed, C. D. Nooijer, M. Jambunathan and S. R. Van, Modeling and characterization of MEMS-based piezoelectric harvesting devices, *J. Micromech. Microeng.* **20** (2010) 105023, doi: 10.1088/0960-1317/20/10/105023.
13. A. Erturk, Electromechanical modeling of piezoelectric energy harvesters, PhD thesis, Virginia Polytechnic Institute and State University, Blacksburg (2009).
14. R. Andosca, T. McDonald, V. Genova, S. Rosenberg, J. Keating, C. Benedixen and J. Wu, Experimental and theoretical studies on MEMS piezoelectric vibrational energy harvesters with mass loading, *Sens. Actuators A* **178** (2012) 76–87.
15. A. V. Quintero, N. Besse, P. Janphuang, R. Lockhart, D. Briand and N. F. Rooij, Design optimization of vibration energy harvesters fabricated by lamination of thinned bulk-PZT on polymeric substrates, *Smart Mater. Struct.* **23** (2014) 045041, doi: 10.1088/0964-1726/23/4/045041.
16. J. H. Park, J. Kang, H. Ahn, S. B. Kim, D. Liu and D. J. Kim, Analysis of stress distribution in piezoelectric MEMS energy harvester using shaped cantilever structure, *Ferroelectrics* **409** (2010) 55–61, doi: 10.1080/00150193.2010.487125.